Scilight

Thermal Science and Applications

https://www.sciltp.com/journals/tsa



Article

Ternary Co-Pyrolysis of Arecanut Husk–Sewage Sludge–Red Mud in a Fixed-Bed Reactor: Product Yields, Biochar Characterization, Heavy Metal Immobilization and N/S Pollutant Suppression

K. H. Arunkumar

Department of Mechanical Engineering, School of Engineering and Technology, CMR University, Bangalore 562149, India; arun.k@cmr.edu.in

How To Cite: Arunkumar, K.H. Ternary Co-Pyrolysis of Arecanut Husk–Sewage Sludge–Red Mud in a Fixed-Bed Reactor: Product Yields, Biochar Characterization, Heavy Metal Immobilization and N/S Pollutant Suppression. *Thermal Science and Applications* **2026**, *1*(4), 341–357. https://doi.org/10.53941/tsa.2026.100021

Received: 20 May 2026
Revised: 10 August 2026
Accepted: 17 September 2026
Published: 22 October 2026

Abstract: Pyrolysis-based valorization of sewage sludge (SS) is limited by the low surface area and elevated ecological risk of the resulting biochar. This study investigated ternary co-pyrolysis of arecanut husk (ANH), municipal SS, and red mud (RM) in a fixed-bed reactor under N_2 and CO_2 atmospheres at 500–600 °C, to increase biochar surface area, lower heavy-metal ecological risk, and enhance hydrogen production. ANH supplied a lignocellulosic meso-channel template and high volatile matter (65.8 wt%), while RM ($Fe_2O_3 \geq 62$ wt%) catalyzed pore development and helped immobilize heavy metals originating from SS. At the optimum condition (15% RM, N_2, 500 °C), biochar surface area reached 184.6 m^2/g, 2.71 times greater than the pure-SS baseline (68.2 m^2/g); CO_2 activation at 600 °C increased this further to 224.8 m^2/g. The Hakanson Ecological Risk Index fell from 495.4 (pure SS) to 98.6 at 15% RM, meeting the EU Biochar Certificate threshold (RI < 150) for unrestricted agricultural use. Under CO_2 at 500 °C, hydrogen yield reached 10.42 mmol/g, while NH_3 and SO_2 emissions fell by 61.3% and 54.8%, respectively, relative to the pure-SS baseline. Multi-response desirability optimization identified 15% RM, N_2, 500 °C as the overall optimum among the conditions tested (D = 0.847). To the authors' knowledge, few studies have examined ternary co-pyrolysis systems combining agricultural, municipal, and industrial waste streams under both inert and CO_2-assisted atmospheres; these findings show that red mud addition can simultaneously improve biochar porosity, reduce ecotoxicological risk, and enhance hydrogen co-production from a ternary waste-derived feedstock.

Keywords: ternary co-pyrolysis; arecanut husk; sewage sludge; red mud; biochar; ecological risk; hydrogen yield; heavy metal immobilization

1. Introduction

Co-pyrolysis of agricultural residues, municipal wastewater sludge (SS), and industrial solid byproducts simultaneously has been proposed by [1,2] as an attractive circular economy solution. Improperly managed sewage sludge adds up to >50 million dry ton/year globally, with municipal SS posing unique challenges due to its high metal content (Cu, Pb, Zn, Cd), high water content, and regulatory restrictions on land use [3–5]. Sludge-derived materials have accordingly been explored across a range of environmental applications [6,7].

The pyrolysis of sewage sludge produces biochar, bio-oil, and syngas. The char also generates partial immobilization of heavy metals through retention in the char phase. However, the physical limitations of the

Copyright: © 2026 by the authors. This is an open access article under the terms and conditions of the Creative Commons Attribution (CC BY) license (https://creativecommons.org/licenses/by/4.0/).
Publisher's Note: Scilight stays neutral with regard to jurisdictional claims in published maps and institutional affiliations.

generated biochar (low BET surface area (S_{BET} < 80 m^2/g) and elevated Hakanson Ecological Risk Index (RI) values (above 300)) make it less useful for either agronomy or the environment [4,8–10].

Arecanut husk (ANH) constitutes the single largest agricultural solid waste stream (approximately 300,000 tons/year, dry basis) produced in coastal Karnataka, India [11]. Its lignocellulosic nature (cellulose 35.4%, hemicellulose 19.2%, and lignin 28%) [12] leads to a high volatile-matter co-feedstock (VM = 65.8 wt%) that will enhance the production of gas from the pyrolysis process and form a fibrous meso-channel template within the co-pyrolysis char matrix.

Red mud (RM) is generated worldwide as a by-product of the Bayer alumina refining process, at approximately 120 million metric tons each year. This alkaline solid residue is composed mainly of iron, containing a high concentration of iron oxide (Fe_2O_3 > 62 wt%). The scale at which RM is produced and stored poses a significant risk to the environment [9], motivating alternative valorization routes such as ceramics and glazes [13]. The iron oxide in RM under controlled conditions of pyrolysis will undergo reduction ($Fe_2O_3 \rightarrow Fe_3O_4 \rightarrow FeO$), this process creates lattice contractions that form mesopores, while acting both as a catalyst for water-gas shift (WGS) reactions and as a chemical sorbent for N and S pollutant gases [2,14]

In addition to being a waste product, RM can function as a catalyst for biochar production or as an enhancer of bio-oil yields from the co-pyrolysis of sludge (SS) and biomass [4,15]. Substantially, 10% of the RM in an SS/biomass binary system had a specific BET surface area of 142.6 m^2/g and a reduced RI of 186.4 (Moderate Risk), so RM acts as both a catalyst and an immobilizing agent [2]. However, no investigation to date has examined the hypothesized ternary system of ANH, SS and RM, which is postulated to provide substantial synergistic benefits not achieved in any of the studied binary subsystems. We hypothesize that the ANH meso-channel template amplifies RM-induced pore development beyond binary-system levels, and that the ANH volatile-matter pool elevates H_2 yield through enhanced Boudouard and WGS reactions; these mechanisms are examined against the experimental results in Section 3.

To the authors' knowledge, few studies have investigated ternary co-pyrolysis systems combining arecanut husk, sewage sludge, and red mud under both N_2 pyrolysis and CO_2-assisted activation. Previous studies have primarily focused on binary systems, including sewage sludge-red mud or biomass-sewage sludge mixtures [2]. The present work extends these studies by systematically evaluating the coupled effects of ternary blending, red mud loading, and process atmosphere on biochar surface area, heavy metal fractionation, ecological risk, syngas quality, and N/S pollutant suppression.

The objectives of this research are as follows: (i) to characterize the co-pyrolysis system of the three feedstocks and the thermogravimetric interaction between those; (ii) to quantify how the amount of red mud (0–20 wt%), pyrolysis temperature (500–600 °C) and atmosphere (N_2/CO_2) impact product yield and biochar characteristics; (iii) to evaluate the fractionation of heavy metals and the ecological risks associated with them using BCR sequential extraction and Hakanson risk assessment methodology; (iv) to characterize the chemical composition of the syngas produced from the three feedstocks and measure the amount of H_2 produced from that syngas; and (v) to determine the amount of carbon in the biochar produced from the co-pyrolysis of the three feedstocks.

2. Materials and Methods

2.1. Feedstock Collection and Preparation

Shimoga District in Karnataka India, ANH was collected from areca-processing farms; then it was sun dried (≤10% moisture), and ground to <2 mm particles size. Dewatered cake form of municipal sewage [16] was supplied as sludge; provided by Doddaballapura Sewage Treatment Plant, Bangalore City, India. Red mud was obtained from Vedanta Aluminium Ltd. (Lanjigarh, Odisha) with Fe_2O_3 concentration (by weight) >62% and pH = 10.8–11.2. All feedstocks prepared used for ANH combustibility testing were dried in an oven at 105 °C for 24 h, stored in sealed container under nitrogen [17].

2.2. Feedstock Characterisation

Proximate analysis performed using ASTM D7582-12 (TGA/SDT Q600, TA Instruments (a subsidiary of Waters Corporation), New Castle, DE, USA). Ultimate analysis (C, H, N, S, and O calculated by difference) conducted according to the ASTM D5373 (CHNS-analyser—Elementar Vario EL III, Elementar Analysensysteme GmbH, Langenselbold, Germany) with the HHV calculated from the ultimate analysis data using the Dulong formula. Heavy metal content in the feedstock determined through an inductively coupled plasma-optical emission spectrometer (ICP-OES) (Optima 7300 DV, PerkinElmer Inc., Waltham, MA, USA) after aqua regia microwave digestions (EPA Method 3051A). Thermo-gravimetric analyses performed at heating rates of 5, 10, 20, and 40 °C/min; those ranged from 30 °C to 800 °C with controlled N_2 or CO_2 gas flow rate of 50 mL/min (TGA Q50;

TA Instruments, a subsidiary of Waters Corporation, New Castle, DE, USA). The experimental data obtained are tabulated in Table 1. Isoconversional activation energies were calculated from these multi-heating-rate data using the FWO [18,19], KAS [20,21] and Starink [22] methods (Supplementary Table S4).

Table 1. Proximate and ultimate analysis of ANH, SS, and RM feedstocks (dry basis, mean ± SD, n = 3).

Parameter	ANH (Mean ± SD)	SS (Mean ± SD)	RM (Mean ± SD)	Unit
Moisture (a.r.)	7.8 ± 0.2	72.4 ± 1.8	18.6 ± 0.4	wt%
Volatile Matter	65.8 ± 1.2	48.6 ± 0.9	1.8 ± 0.1	wt% d.b.
Fixed Carbon	22.5 ± 0.5	10.3 ± 0.3	12.5 ± 0.3	wt% d.b.
Ash	11.7 ± 0.4	41.1 ± 0.8	85.7 ± 1.2	wt% d.b.
Carbon (C)	47.8 ± 0.6	23.4 ± 0.5	1.2 ± 0.1	wt% d.b.
Hydrogen (H)	6.1 ± 0.1	3.8 ± 0.1	0.4 ± 0.0	wt% d.b.
Nitrogen (N)	0.8 ± 0.0	4.8 ± 0.1	0.3 ± 0.0	wt% d.b.
Sulphur (S)	0.2 ± 0.0	1.6 ± 0.1	0.2 ± 0.0	wt% d.b.
Oxygen (by diff.)	33.4	25.3	12.2	wt% d.b.
HHV	18.42 ± 0.32	11.34 ± 0.28	0.84 ± 0.02	MJ/kg
H/C atomic ratio	1.53	1.95	—*	—
O/C atomic ratio	0.52	0.81	—*	—

d.b. = dry basis; a.r. = as-received; HHV calculated by Dulong correlation. * Not reported for RM: because RM contains only trace amounts of carbon, the calculated H/C and O/C atomic ratios are numerically large and of limited physicochemical significance, and are not interpretable in the same manner as those of lignocellulosic feedstocks.

2.3. Pyrolysis Experiments

A schematic diagram of the reactor configuration is shown in Figure 1. In a horizontal fixed bed quartz reactor (50 mm inner diameter, 400 mm heated length) (Lindberg/Blue M STF55346C tube furnace, Thermo Fisher Scientific Inc., Waltham, MA, USA), studies were conducted to determine the co-pyrolysis of feedstock blends (10.0 g total, dry weight basis) consisting of a combination of RM with 0%, 5%, 10%, 15%, and 20% (w/w) of RM to make a layered ternary blend, where the remainder of the mass was composed of an ANH:SS in a 1:1 ratio. The 1:1 ANH:SS ratio was fixed throughout so that RM loading, temperature, and atmosphere could each be varied independently against a single, constant organic-feedstock baseline; this ratio was chosen as a simple, reproducible baseline balancing ANH's high volatile-matter content against SS's higher ash and heteroatom (N, S) content, rather than to represent a specific real-world co-disposal ratio. R1 contained only ANH and R2 contained SS alone. The remaining eleven runs (R3–R13) comprised 1:1 ANH:SS blends with 0, 5, 10, 15, or 20 wt% RM; each RM loading was run under both N_2 and CO_2 at 500 °C, except 20% RM (R12), which was run under N_2 only. R13 repeated the 15% RM, CO_2 condition at 600 °C. R3 was a preliminary screening run (product yield only); R4 served as the fully-characterized 0% RM control. The complete experimental matrix, including composition, temperature, atmosphere, and the characterization performed for each run, is given in Table 2. Figure 1 is the schematic diagram of reactor system.

Table 2. Product yields (char, bio-oil, gas) for all thirteen experimental runs; char fuel properties (HHV, H/C, O/C) are reported for the subset of samples selected for full ultimate analysis (mean ± SD, n = 3).

Sample ID	Condition	Char Yield (%)	Bio-Oil Yield (%)	Gas Yield (%)	Char HHV (MJ/kg)	H/C Atomic	O/C Atomic
R1	ANH only, N_2, 500 °C	42.8 ± 0.6	21.4 ± 0.5	35.8 ± 0.7	22.84 ± 0.38	0.48	0.13
R2	SS only, N_2, 500 °C	54.2 ± 0.8	18.4 ± 0.4	27.4 ± 0.6	18.62 ± 0.29	0.75	0.29
R3	0% RM (screening), N_2, 500 °C	48.6 ± 0.7	20.1 ± 0.5	31.3 ± 0.6	21.46 ± 0.34	0.61	0.21
R4	0% RM (control), N_2, 500 °C	47.2 ± 0.6	20.8 ± 0.4	32.0 ± 0.5	22.84 ± 0.32	0.48	0.13
R5	0% RM (control), CO_2, 500 °C	45.8 ± 0.7	19.6 ± 0.5	34.6 ± 0.6	23.42 ± 0.35	0.43	0.11
R6	5% RM, N_2, 500 °C	47.9 ± 0.6	20.6 ± 0.4	31.5 ± 0.6	—	—	—
R7	5% RM, CO_2, 500 °C	46.6 ± 0.7	19.8 ± 0.5	33.6 ± 0.7	—	—	—
R8	10% RM, N_2, 500 °C	45.9 ± 0.6	20.3 ± 0.4	33.8 ± 0.6	—	—	—
R9	10% RM, CO_2, 500 °C	44.8 ± 0.7	19.7 ± 0.5	35.5 ± 0.7	—	—	—
R10	15% RM, N_2, 500 °C	43.6 ± 0.6	21.2 ± 0.4	35.2 ± 0.7	24.68 ± 0.36	0.34	0.08
R11	15% RM, CO_2, 500 °C	42.1 ± 0.5	20.4 ± 0.4	37.5 ± 0.7	25.14 ± 0.40	0.30	0.07
R12	20% RM, N_2, 500 °C	41.5 ± 0.6	20.8 ± 0.4	37.7 ± 0.7	—	—	—
R13	15% RM, CO_2, 600 °C	38.6 ± 0.5	19.8 ± 0.3	41.6 ± 0.8	26.18 ± 0.42	0.21	0.05

HHV = higher heating value; H/C and O/C calculated on dry ash-free basis.

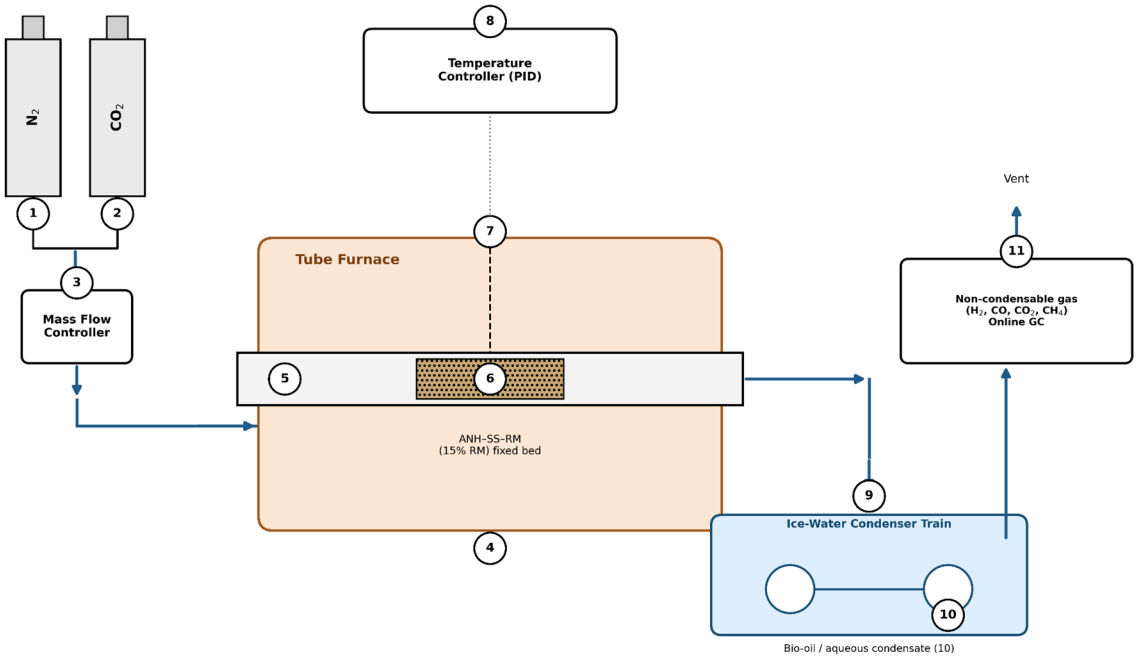


Figure 1. Schematic diagram of the horizontal fixed-bed reactor system used for the co-pyrolysis experiments, showing feedstock loading, carrier-gas (N_2/CO_2) supply, heated zone, and gas train to GC/TG-FTIR analysis.

The components in the schematic are (1) N_2 cylinder; (2) CO_2 cylinder; (3) mass flow controller; (4) tube furnace; (5) fixed-bed reactor tube; (6) ANH–SS–RM sample bed; (7) thermocouple; (8) PID temperature controller; (9) ice-water condenser train; (10) bio-oil/aqueous condensate collection; (11) non-condensable gas collection and online GC analysis (H_2, CO, CO_2, CH_4).

The reactor was heated to either 500 or 600 degrees Celsius at a rate of 20 degrees Celsius/min and once the desired temperature was reached was maintained at that temperature for 60 min with a flow of 200 mL/min of carrier gas (either N_2 or CO_2, 99.999% purity) through it. A two-stage ice-cooled trap was used to collect the condensate (bio-oil and aqueous phase) and non-condensable gas was collected in a 5-litre Tedlar bag. The char yield was determined gravimetrically. Note that GC-MS characterization of bio-oil was not completed as part of the study and should be part of future research. All tests were conducted in triplicate (n = 3), and results are reported as mean ± SD.

2.4. Biochar Characterisation

The BET surface area (S_{BET}), total pore volume (Vtotal), micropore volume (Vmicro) and pore size distribution were measured using nitrogen adsorption and desorption at 77K with a Micromeritics ASAP 2020, Micromeritics Instrument Corp., Norcross, GA, USA. Figure 2 gives the details of BET Surface and pore size distribution. The samples were degassed for twelve hours at 300° Celsius before analysis took place and followed IUPAC 2015 isotherm classification guidelines. X-ray diffraction (XRD) was performed on a Rigaku MiniFlex 600 diffractometer, Rigaku Corporation, Tokyo, Japan (CuKα, λ = 0.154 nm, 2θ = 5–80°, Step = 0.02°). FTIR Spectroscopy was performed using a Thermo Nicolet iS10 ATR-FTIR Spectrometer, Thermo Fisher Scientific Inc., Waltham, MA, USA (4000–400 cm^{-1} 32 Scans, 4 cm^{-1} Resolution) and Raman Spectroscopy on Renishaw inVia Reflex Raman Spectrometer, Renishaw plc, Wotton-under-Edge, Gloucestershire, UK (532 nm, 10 mW, 50× Objective, 10 Accumulations) to measure D/G band ratio using single peak height measurements and baseline corrected data.

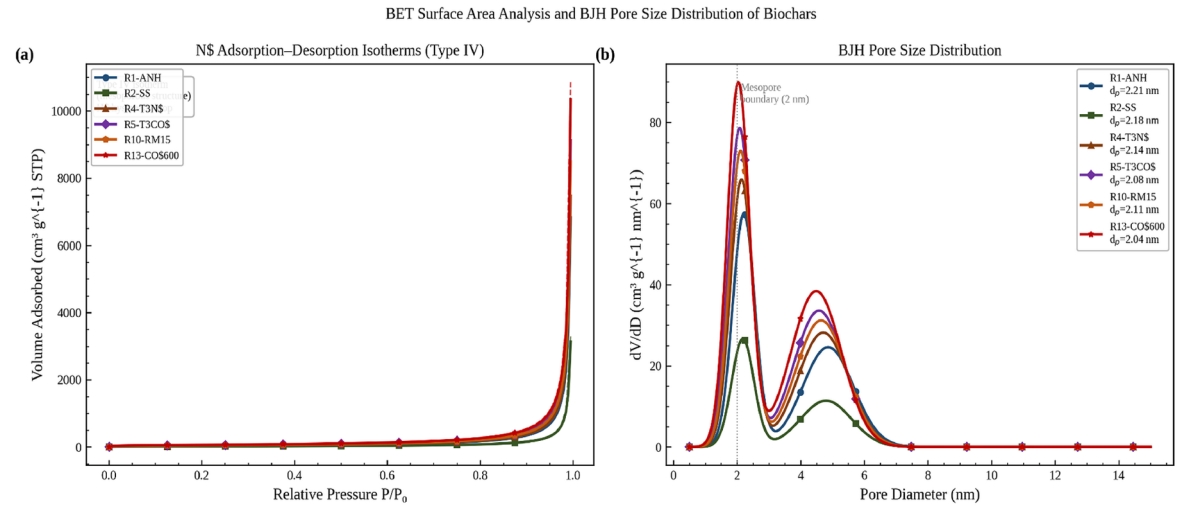


Figure 2. BET N_2 adsorption–desorption isotherms and pore size distribution for selected biochar samples (R2, R4, R10, R13). Error bars represent ± SD (n = 3). All samples exhibit Type I/IV mixed isotherms (IUPAC 2015) with H4 hysteresis loops, consistent with combined micropore–mesopore character.

2.5. Structural Characterisation

Structural evolution of the biochar was evaluated using N_2 adsorption–desorption (BET), X-ray diffraction (XRD), Fourier-transform infrared spectroscopy (FTIR), Raman spectroscopy, and pore-size distribution analysis. These techniques provide information on specific surface area, pore characteristics, mineral phases, functional groups, and carbon structural ordering. No direct microscopic characterization (e.g., SEM-EDS) was performed in the present study. Consequently, the discussion of pore morphology and mineral distribution in Section 3.2 is presented as an interpretation derived from the combined analytical evidence and relevant literature, rather than as a direct microscopic observation. Figure 3 provides a conceptual schematic of the proposed morphological evolution of four representative samples. It shows the expected correspondence with the characterization data, not a direct microscopic observation; acquisition of SEM-EDS equipment for direct morphological validation is identified as a priority for future work.

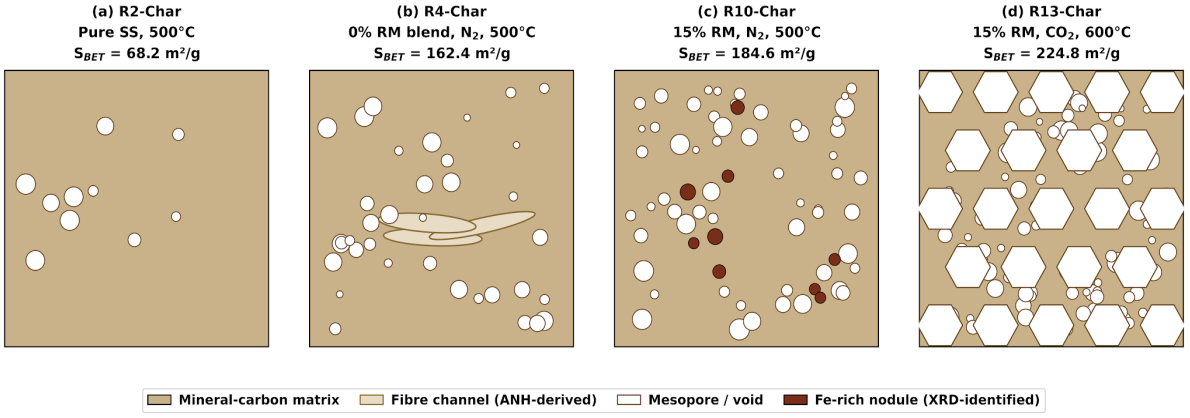


Figure 3. Conceptual schematic of the proposed morphological evolution of four representative chars (R2, R4, R10, R13). The panels show the expected correspondence with the BET, XRD, and FTIR characterization data. This is a conceptual diagram, not a micrograph: no SEM-EDS imaging was performed in this study (Section 2.5).

2.6. Heavy Metal Fractionation and Ecological Risk Assessment

The BCR stepwise extraction was designed based on the method description provided in [23] (see Supplementary Material, Text S1 for the full methodology). There were four fractions extracted from the samples (F1—exchangeable/acid-soluble (0.11 M acetic acid), F2—reducible (0.5 M hydroxylamine hydrochloride at a pH of 2), F3—oxidizable (H_2O_2 followed by 1.0 M ammonium acetate at a pH of 2), and F4—residual (aqua regia microwave digestion)). The metal concentrations in each of the fractions were analyzed using ICP-OES analysis. The mobility factor (MF%) was calculated as [(F1 + F2)/(F1 + F2 + F3 + F4)] × 100. Hakanson [24] assessed

ecological risk using the monomial potential environmental risk factor E_r^i, where $E_r^i = T_r^i \times Cf^i$, where $Cf^i = C_i/C_{0i}$ (contamination factor) and T_r^i = toxicity response coefficient (Cd = 30; Cu, Pb, Ni = 5; Cr = 2; Zn = 1). The other components of RI = ΣE_r^i for all contaminants present in each site. The Hakanson RI and the EU Biochar Certificate (EBC) threshold serve different purposes: RI is a multi-metal ecological hazard index, while the EBC RI < 150 criterion is a regulatory screening value referenced against it. Meeting the EBC threshold indicates suitability for unrestricted agricultural use under that specific certification scheme, rather than establishing precedence over the wider biochar literature.

2.7. Syngas Analysis

The composition of syngas (H_2, CO, CO_2, CH_4, N_2, and C_2H_x) was quantitatively assessed using dual detector gas chromatography (Shimadzu GC-2014, Shimadzu Corporation, Kyoto, Japan; TCD detector, c/s Ar; 5 Å molecular sieve and Poropak Q columns). The H_2 yield (mmol/g of dry feedstock charged to the reactor) was estimated from the measured H_2 concentration using gas chromatography (GC) calibration curves established with certified standards. Syngas composition was determined from the measured volume fractions of the individual gas components, including H_2, CO, CO_2, CH_4, and C_2H_x. The lower heating value (LHV) of the syngas was not calculated in this study. Evolved gas analysis (EGA) and gas evolution during pyrolysis (NH_3 = 966 cm^{-1}, SO_2 = 1152 cm^{-1}, HCN = 714 cm^{-1}) was accomplished using thermogravimetric analysis coupled to Fourier-transform infrared spectroscopy (TG-FTIR), using a TGA Q50 (TA Instruments, a subsidiary of Waters Corporation, New Castle, DE, USA) connected through a heated transfer line at 220 °C to a Thermo Nicolet iS10 FTIR spectrometer (Thermo Fisher Scientific Inc., Waltham, MA, USA).

2.8. Multi-Response Optimisation

The multi-objective optimization process was carried out using the Derringer-Suich desirability function (Minitab 20, Minitab, LLC, State College, PA, USA). The four response variables were: S_{BET} (maximum), RI (minimum), H_2 yield (maximum), and MF% (minimum). Within each fixed temperature-atmosphere combination, RM loading (0–20%) was the primary variable investigated; temperature and atmosphere effects were evaluated independently by comparing samples with identical blend compositions. Each response criterion was evaluated with an individual desirability function. The overall desirable criterion (D) was determined by multiplying the desirability functions of each response ($d_1 \times d_2 \times d_3 \times d_4$) and raising the result to the 1/4 power. A one-way ANOVA with Tukey HSD post-hoc analysis was performed at $\alpha = 0.05$ to verify significance (see Section 3.7) of RM loading on the composite desirability.

3. Results and Discussion

3.1. Feedstock Properties and Proximate/Ultimate Analysis

The three feedstocks were compared in Table 1 by their proximate and ultimate compositions, and the results show that ANH contains the largest amounts of volatile matter (VM = 65.8 wt% dry basis), characteristic of lignocellulosic biomass, while SS contains the largest amount of ash (41.1 wt%), which consists of inorganic minerals. RM has a small amount of VM (<2 wt%) and is primarily inorganic (residue after 800 °C combustion = 85.7 wt%). The order of carbon content is as follows: ANH (47.8%) > SS (23.4%) > RM (1.2%). The nitrogen and sulphur content was greatest in SS (N = 4.8%, S = 1.6%), which points to some biological protein and fat content in SS. Heating values (HHV) followed the same order, with ANH (18.42 MJ/kg) exceeding SS (11.34 MJ/kg), while RM (0.84 MJ/kg) was lowest, consistent with its predominantly inorganic composition. Energy recovery studies from the ternary mixture had HHV ranging from 22.84 MJ/kg (R4, 0% RM baseline) to 26.18 MJ/kg (R13, CO_2, 600 °C) alongside a shift toward more ordered, graphitic carbon structures, reflected in Raman ID/IG ratios decreasing from 0.92 to 0.71. This range of HHV is comparable to the HHV of subbituminous coal (26–30 MJ/kg), so these feedstocks have potential as solid fuels.

3.2. Biochar Characterisation: Surface Area, Pore Structure, and Spectroscopic Analysis

Table 3 summarizes the BET surface area (S_{BET}), micropore volume (Vmicro), total pore volume (Vtotal), and average pore diameter of the biochar. Pure sewage-sludge (SS) char (R2-Char, 500 °C, N_2) exhibited an S_{BET} of 68.2 ± 1.8 m^2/g and a micropore volume of 0.038 ± 0.002 cm^3/g. In contrast, the 0% red mud (RM) ANH-containing control (R4-Char) exhibited 162.4 ± 3.4 m^2/g and 0.072 ± 0.003 cm^3/g, respectively, highlighting the influence of feedstock composition on porosity.

The N_2 adsorption–desorption isotherms (Figure 2) exhibited Type I/IV characteristics and H4 hysteresis loops [25], consistent with slit-like pores and the possible coexistence of micropores and mesopores. Under N_2 at 500 °C, (S_{BET}) increased from 171.0 ± 4.0 m^2/g at 5% RM (R6-Char) to 184.6 ± 4.1 m^2/g at 15% RM (R10-Char) and 191 ± 5 m^2/g at 20% RM (R12-Char), indicating an overall increase with RM loading.

XRD patterns (Figure 4) showed Fe_3O_4-related reflections at approximately 35.5°, 43.1°, and 57.0°. Iron oxide transformations may contribute to changes in the mineral–carbon matrix and pore development, although a causal relationship requires further evidence. ATR–FTIR spectra (Figure 5) showed bands associated with O–H (3420 cm^{-1}), aliphatic C–H (2920 cm^{-1}), aromatic C=C (1580 cm^{-1}), C–O (1060 cm^{-1}), and Fe–O (560 cm^{-1}) vibrations. Attenuation of the C–H and C–O bands with increasing RM loading and/or temperature is consistent with the decomposition of aliphatic and oxygen-containing groups during pyrolysis. Changes in the Fe–O band may reflect variations in iron-containing phases but do not independently confirm specific oxide transformations.

R13-Char (sewage sludge [26,27] and 15% RM, CO_2, 600 °C) exhibited the highest (S_{BET}) (224.8 ± 5.2 m^2/g), micropore volume (0.104 ± 0.005 cm^3/g), and total pore volume (0.128 ± 0.006 cm^3/g). Its enhanced porosity may reflect the combined effects of feedstock composition, temperature, and CO_2-assisted reactions. Its surface area falls within the reported 100–900 m^2/g range for activated carbons used in water treatment, although application suitability also depends on adsorption performance and surface chemistry.

The Raman (I_D/I_G) ratio decreased from 0.92 (R1-Char) to 0.71 (R13-Char) (Figure S2), suggesting changes in carbon structural organization, but not conclusively establishing graphitization because mineral phases and carbon disorder can influence Raman spectra. HHV increased from 22.84 to 26.18 MJ/kg (Table 2), potentially reflecting compositional changes. Feedstock and char H/C and O/C ratios are presented in the van Krevelen diagram (Figure S1) [28].

Figure 3 presents conceptual morphological interpretations based on BET, XRD, and ATR–FTIR results, not direct imaging. Figure 3a depicts R2-Char (68.2 m^2/g) with relatively restricted accessible porosity; Figure 3b represents R4-Char (162.4 m^2/g); Figure 3c illustrates the proposed pore network of R10-Char (184.6 m^2/g); and Figure 3d depicts the proposed extensive porosity of R13-Char (224.8 m^2/g; total pore volume 0.128 cm^3/g). These interpretations are broadly contextualized by prior studies of SS-derived biochar [5], SS–RM biochar [2], and starch-based activated carbons [29]. As SEM imaging was not performed, the proposed smooth, channeled, and honeycomb-like structures remain conceptual rather than experimentally verified morphologies.

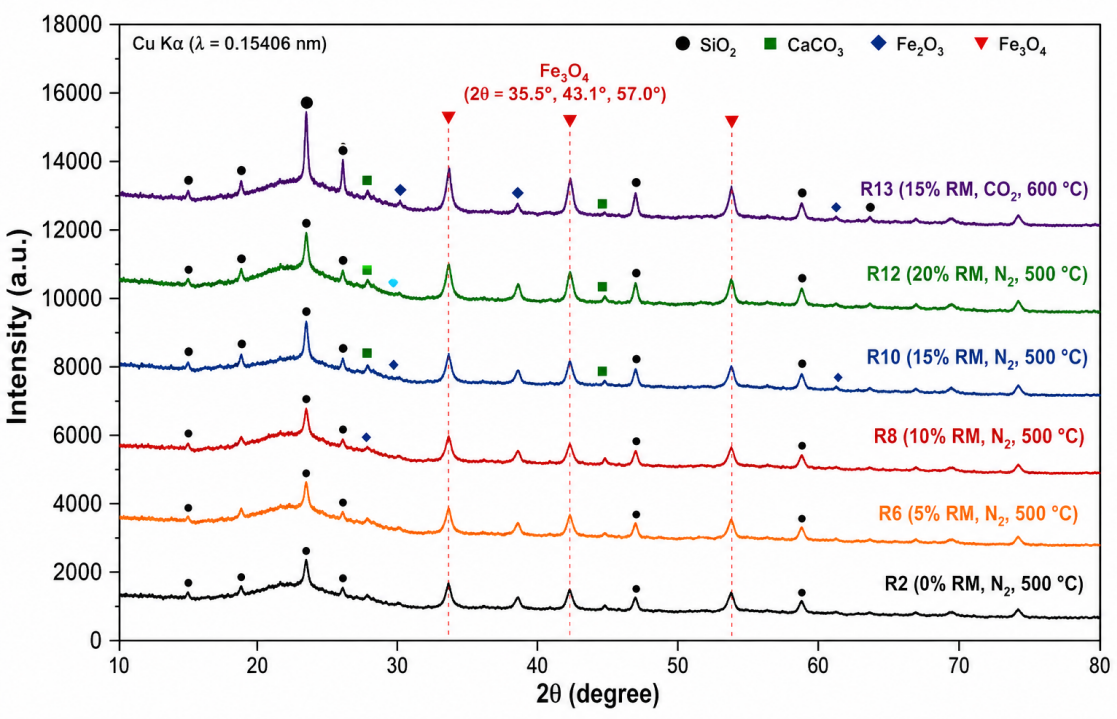


Figure 4. XRD patterns of biochar obtained from sewage sludge (SS) and ANH–SS–RM blends under different red mud (RM) loading and pyrolysis conditions: R2 (SS only, 0% RM, N_2, 500 °C), R5 (5% RM, N_2, 500 °C), R8 (10% RM, N_2, 500 °C), R10 (15% RM, N_2, 500 °C), R12 (20% RM, N_2, 500 °C), and R13 (15% RM, CO_2, 600 °C). Cu Kα radiation (λ = 0.15406 nm) was used. The broad reflection near 25° is associated with turbostratic aromatic carbon, while the mineral phases are represented by SiO_2, Ca-containing phases, and iron oxides. The characteristic Fe_3O_4-related reflections at approximately 35.5°, 43.1°, and 57.0° become evident in the RM-containing samples.

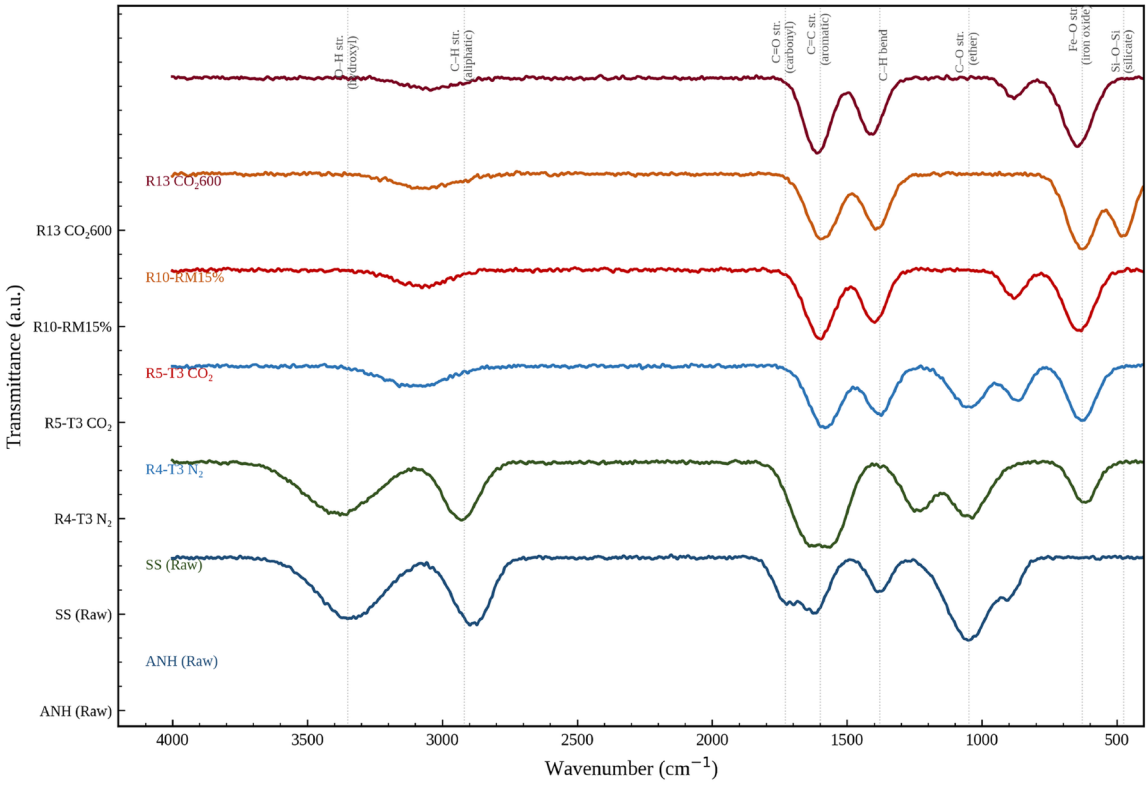


Figure 5. ATR–FTIR spectra of six samples, comprising raw anhydrous sodium hydroxide (ANH), raw sewage sludge (SS), and four biochar samples (R4–T3 N_2, R5–T3 CO_2, R10–RM 15%, and R13–CO_2 600). The characteristic absorption bands are observed at approximately 3420 cm^{-1} (O–H stretching), 2920 cm^{-1} (aliphatic C–H stretching), 1580 cm^{-1} (aromatic C=C stretching), 1060 cm^{-1} (C–O stretching in ether/cellulosic structures), and 560 cm^{-1} (Fe–O stretching in iron-containing phases). Variations in band intensity and position reflect changes in surface functional groups and mineral phases associated with feedstock composition and pyrolysis conditions.

Table 3. BET surface area for eleven biochar samples; full pore-structure data (micropore/total pore volume, average pore diameter, isotherm type) are reported for the six samples selected for detailed textural characterization (mean ± SD, n = 3).

Sample	Condition	S_BET (m^2/g)	V_Micro (cm^3/g)	V_Total (cm^3/g)	D_Avg (nm)	Isotherm Type
R2-Char	SS, N_2, 500 °C	68.2 ± 1.8	0.038 ± 0.002	0.062 ± 0.003	3.6	Type I/IV, H4
R4-Char	0% RM (control), N_2, 500 °C	162.4 ± 3.4	0.072 ± 0.003	0.094 ± 0.004	2.3	Type I/IV, H4
R5-Char	0% RM (control), CO_2, 500 °C	178.3 ± 3.8	0.081 ± 0.003	0.106 ± 0.004	2.4	Type I/IV, H4
R6-Char	5% RM, N_2, 500 °C	171 ± 4	—	—	—	—
R7-Char	5% RM, CO_2, 500 °C	186 ± 4	—	—	—	—
R8-Char	10% RM, N_2, 500 °C	176 ± 4	—	—	—	—
R9-Char	10% RM, CO_2, 500 °C	191 ± 4	—	—	—	—
R10-Char	15%RM, N_2, 500 °C	184.6 ± 4.1	0.088 ± 0.004	0.112 ± 0.005	2.4	Type I/IV, H4
R11-Char	15%RM, CO_2, 500 °C	198.2 ± 4.6	0.094 ± 0.004	0.118 ± 0.005	2.4	Type I/IV, H4
R12-Char	20% RM, N_2, 500 °C	191 ± 5	—	—	—	—
R13-Char	15%RM, CO_2, 600 °C	224.8 ± 5.2	0.104 ± 0.005	0.128 ± 0.006	2.3	Type I/IV, H4

V_micro = micropore volume (t-plot); V_total at P/P_0 = 0.99; D_avg = 4V_total/S_BET.

3.3. Product Yields

As the temperature and the amount of red mud (RM) increase, the char yield decreases from 54.2% at R2 (SS alone) to 38.6% at R13 (15% RM, CO_2, 600 °C) (see Table 2). The maximum yields of bio-oil reported is 21.4% with gas yields in the range of 27.4% to 41.6%. Compared to N_2, the CO_2 atmosphere reduced bio-oil yield by 3–6% (relative) and increased gas yield by 1.7–2.6 percentage points across the RM loadings tested (R4/R5, R6/R7, R8/R9, and R10/R11 pairs; Table 2). This is consistent with the Boudouard reaction, which consumes char carbon and produces carbon monoxide (CO). The use of ANH in combination with SS produced an increase of 5.1 pp in the yield of gas compared to the use of SS alone due to the high volatile matter content (65.8 wt%) present in ANH. The yield of the solid products from the co-addition of ANH and SS is consistent with the thermogravimetric analysis (shown in Table S2), with ANH exhibiting decomposition primarily between 220 and 520 °C (DTG_{max} = −8.42% min^{-1}) and SS between 240 and 620 °C. Synergy between ANH and SS was assessed by comparing

experimental blend yields against theoretical values calculated as the mass-weighted average of the single-feedstock yields (R1, R2) at the 1:1 ANH:SS ratio: theoretical char, bio-oil, and gas yields were 48.5%, 19.9%, and 31.6%, respectively. The experimental values for the 0% RM blend were close to additive for the preliminary screening run (R3: char 48.6%, bio-oil 20.1%, gas 31.3%; deviations of +0.2%, +1.0%, and −0.9%) and showed a small synergistic deviation for the characterized control (R4: char 47.2%, bio-oil 20.8%, gas 32.0%; deviations of −2.7%, +4.5%, and +1.3%), indicating a modest positive synergy in bio-oil formation rather than a purely additive blend.

3.4. Ecological Risk Assessment and Heavy Metal Fractionation

BCR sequential extraction results (Figure 6) demonstrate changes in heavy-metal partitioning with RM addition, including reductions in the exchangeable/acid-soluble (F1) and reducible (F2) fractions and increased contributions from the residual (F4) fraction for several metals. The mobile fraction (MF) of Cd decreased from 47.8% in R2 (pure SS) to 19.0% in R10 (15% RM), while that of Zn declined from 58.4% to 33.0%. These changes suggest reduced metal mobility, potentially through precipitation, surface complexation, and interactions with iron-containing mineral phases. The increased BET surface area of RM-containing chars (Table 3) may also favor metal retention; however, Figure 6 represents metal fractionation rather than direct adsorption or surface-area measurements, and the proposed mechanisms require further verification.

The Hakanson ecological risk index (RI) (Figure 7) decreased from 495.4 for R2 to 310.8 for R4 (0% RM control), 218.4 for R5 (CO_2, 500 °C), and 98.6 for R10 (15% RM). The RI of R10 falls below the threshold of 150 cited in the risk assessment [30], indicating substantially lower potential ecological risk under the investigated conditions. However, this result alone does not establish suitability for unrestricted agricultural use, which requires compliance with applicable certification criteria, including limits on total metal concentrations and leaching behavior. Overall, the results indicate that RM addition can reduce heavy-metal mobility and calculated ecological risk in the investigated biochar.

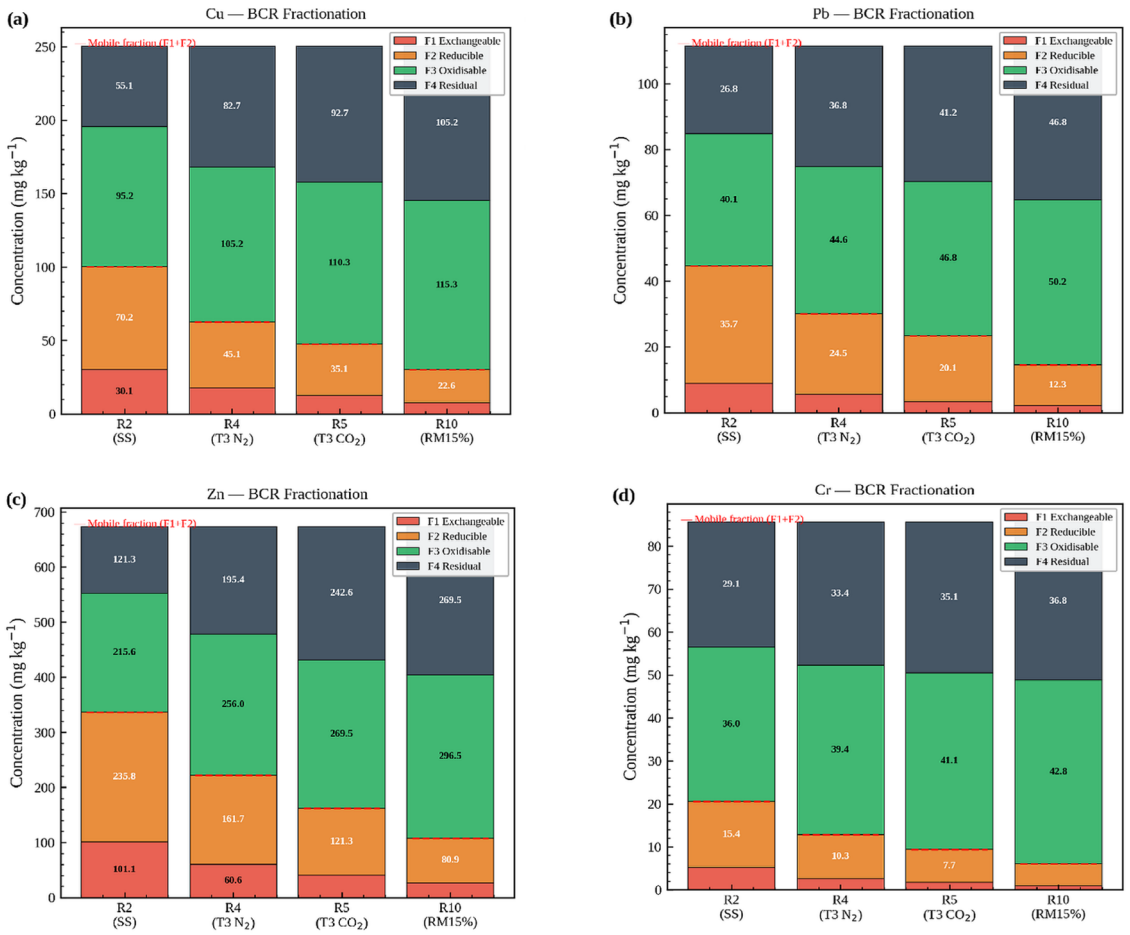


Figure 6. *Cont.*

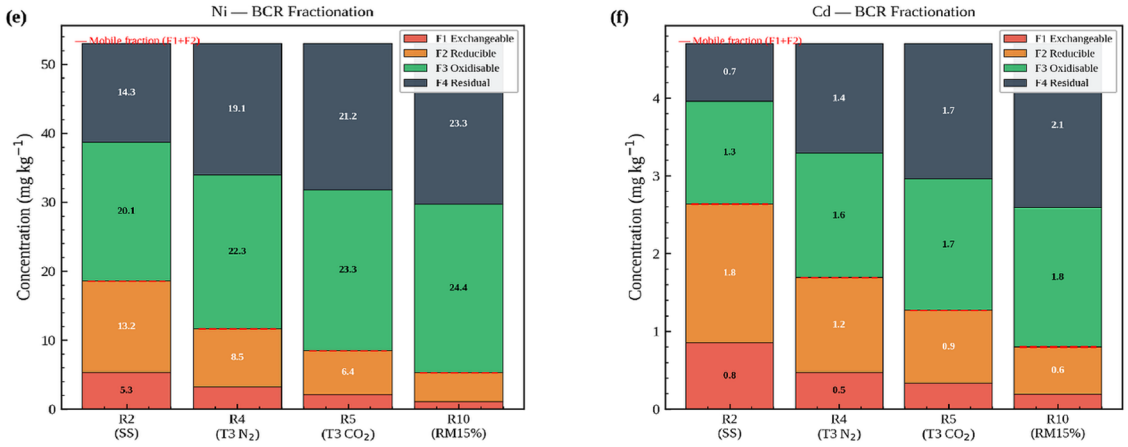


Figure 6. BCR sequential extraction fractions (F1–F4, %) for Cu, Pb, Zn, Cd across six char samples (R2, R4, R5, R10, R11, R13). Error bars: ± SD (n = 3). Progressive reduction in F1 (exchangeable) and F2 (reducible) fractions with RM loading confirms heavy metal immobilization.

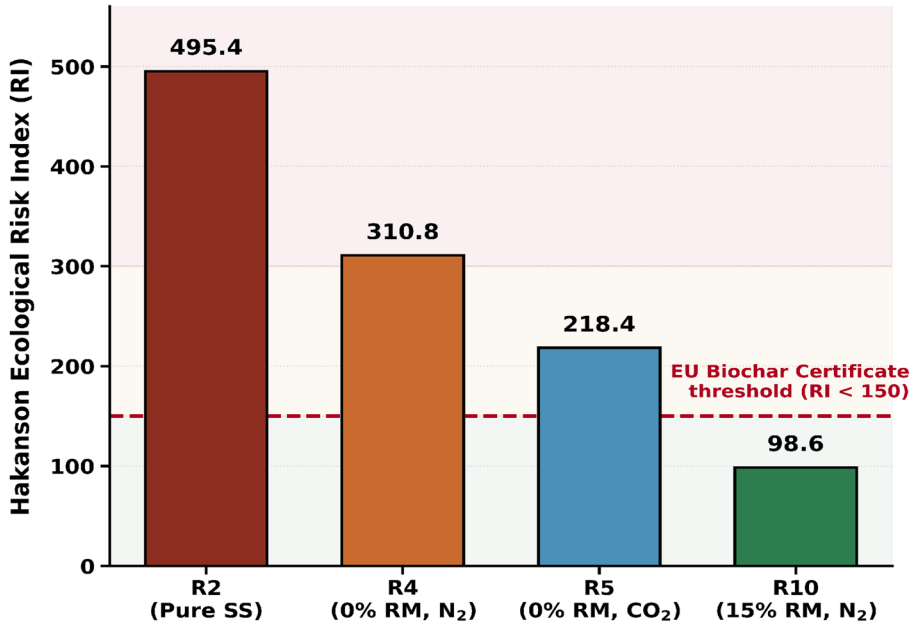


Figure 7. Hakanson potential ecological risk index (RI) for all biochar samples as a function of RM loading. Error bars: ± SD (n = 3). Horizontal dashed lines indicate RI classification boundaries (Low: < 150; Moderate: 150–300; Considerable: 300–600). EU Biochar Certificate threshold (RI < 150) shown as dotted red line.

3.5. Syngas Characterisation and H_2 Yield

H_2 syngas yields were determined as a function of red mud [14] (RM) loading and temperature, given thermal conversion of RM under either an N_2 (R2, SS only) or CO_2 (R13) atmosphere, as shown in Figure 8 and Table 4. Under the N_2 atmosphere at 500 °C, H_2 production from 4.82 mmol/g (R2, SS only) to 8.74 mmol/g (R10, 15% RM) resulted from the $CO + H_2O \rightleftharpoons CO_2 + H_2$ reaction catalyzed by iron phases of RM, specifically when operating under N_2 at 500 °C. Under the CO_2 atmosphere at a 600 °C reaction temperature (R13), H_2 production was highest (10.42 mmol/g), representing a 30% increase over N_2 at its highest yield, due to both use of the Boudouard reaction ($C + CO_2 \rightleftharpoons 2CO$) and subsequent WGS. This considerable increase in the yield of H_2 syngas resulted in a decrease of the syngas CO_2/CO (Figure 9), with the ratio reducing from 2.1 at N_2 (500 °C) to 0.3 at CO_2 (600 °C) indicating that the rate of carbon gasification was increased when combusting RM in a CO_2 atmosphere. The yield of CH_4 was less than 1.2 mmol/g throughout all reaction environments.

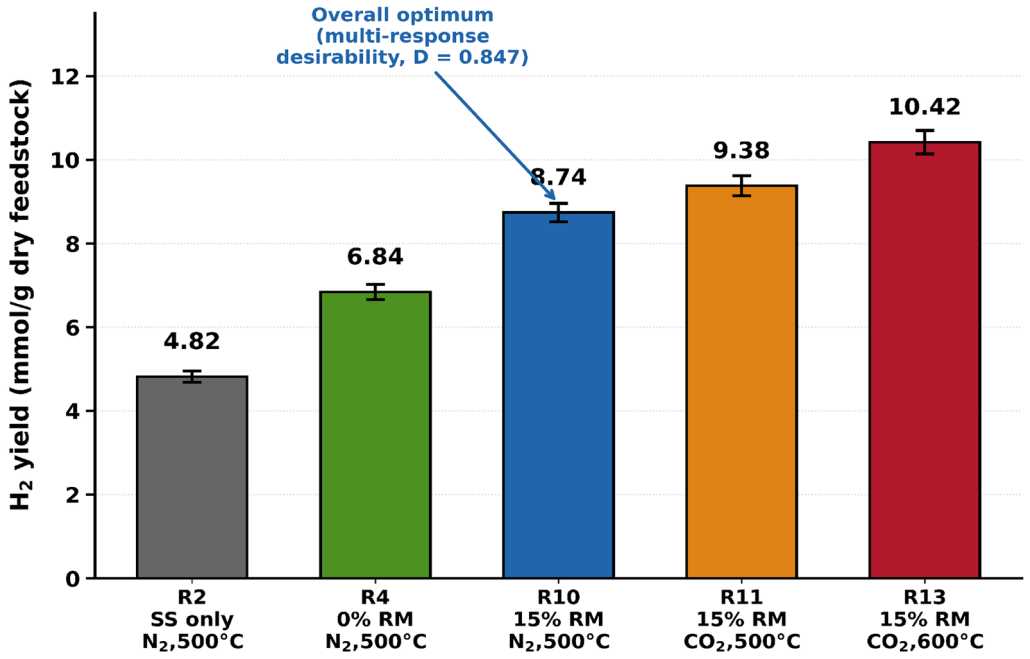


Figure 8. H_2 yield of selected biochar-producing conditions under N_2 and CO_2 atmospheres at 500 and 600 °C. Error bars represent ± SD (n = 3). The maximum measured H_2 yield was 10.42 ± 0.28 mmol g^{-1} for R13 (15% RM, CO_2, 600 °C). The overall multi-response desirability was D = 0.847 at 15% RM.

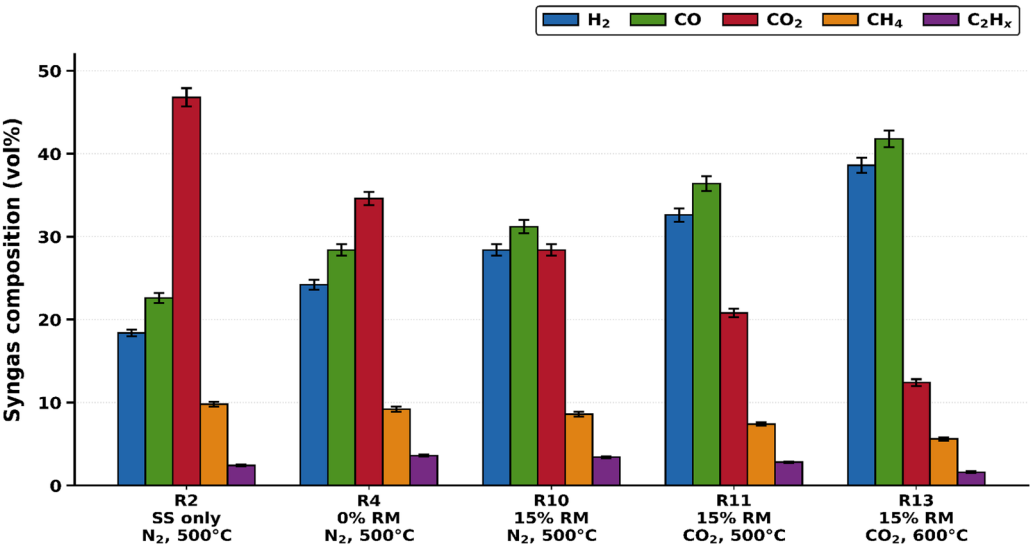


Figure 9. Syngas composition (H_2, CO, CO_2, CH_4, C_2H_x, vol%) under N_2 and CO_2 atmospheres at 500 °C and 600 °C for the optimal blend (T3, 15% RM). Error bars: ± SD (n = 3).

Table 4. Syngas composition (vol%) and H_2 yield (mmol/g) under selected conditions (mean ± SD, n = 3).

Sample	Condition	H_2 (vol%)	CO (vol%)	CO_2 (vol%)	CH_4 (vol%)	C_2H_x (vol%)	H_2 Yield (mmol/g)	CO_2/CO Ratio
R2	SS only, N_2, 500 °C	18.4 ± 0.4	22.6 ± 0.6	46.8 ± 1.1	9.8 ± 0.3	2.4 ± 0.1	4.82 ± 0.14	2.1
R4	T3, N_2, 500 °C	24.2 ± 0.6	28.4 ± 0.7	34.6 ± 0.8	9.2 ± 0.3	3.6 ± 0.1	6.84 ± 0.18	1.2
R10	15%RM, N_2, 500 °C	28.4 ± 0.7	31.2 ± 0.8	28.4 ± 0.7	8.6 ± 0.3	3.4 ± 0.1	8.74 ± 0.22	0.9
R11	15%RM, CO_2, 500 °C	32.6 ± 0.8	36.4 ± 0.9	20.8 ± 0.5	7.4 ± 0.2	2.8 ± 0.1	9.38 ± 0.24	0.6
R13	15%RM, CO_2, 600 °C	38.6 ± 0.9	41.8 ± 1.0	12.4 ± 0.4	5.6 ± 0.2	1.6 ± 0.1	10.42 ± 0.28	0.3

WGS = water–gas shift reaction. Boudouard reaction active under CO_2 atmosphere at ≥ 500 °C.

3.6. N/S Pollutant Suppression

Co-pyrolysis of RM (15%) with SS resulted in a significant decrease (−61.3% and −54.8% for NH_3 and SO_2, respectively) in emissions of both gases, which may be associated with catalytic interactions involving Fe-rich mineral phases in red mud (RM), potentially including $Fe_2O_3 + 3H_2S \rightarrow 2FeS + S + 3H_2O$ and $3Fe_2O_3 + 10NH_3 +$

→ $2Fe_3N + 9H_2O + 7N_2$, together with chemical absorption of SO_2 ($CaO + SO_2 + 0.5O_2 \rightarrow CaSO_4$) by alkaline RM phases (e.g., CaO, Na_2O). These iron nitride/sulfide phases were not directly identified in the present study and are proposed only as plausible mechanisms requiring confirmation by techniques such as XPS, SEM-EDS, Mössbauer spectroscopy, or X-ray absorption spectroscopy. At all conditions, HCN formation was not evaluated quantitatively in the present study because the reported TG–FTIR analysis focused on H_2O, CO_2, NH_3, and SO_2 (Figures 10 and 11). Therefore, HCN emissions cannot be confirmed as negligible, and no conclusion regarding HCN release relative to the total nitrogen budget can be drawn from the available measurements.

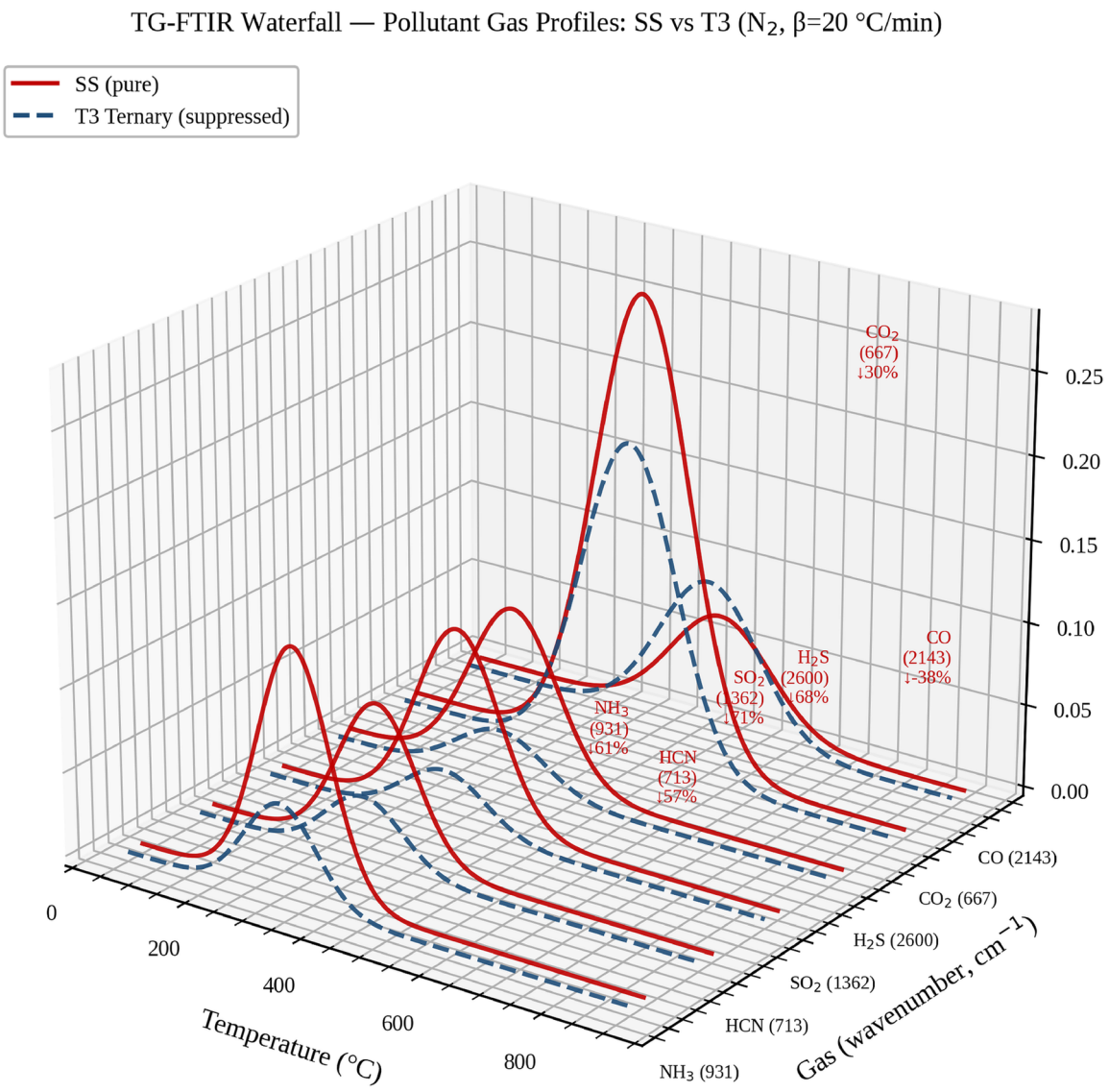


Figure 10. TG-FTIR 3D waterfall plots of evolved gas absorbance profiles during co-pyrolysis of ANH–SS–RM ternary blends at 500 °C under N_2. Key bands: 3340 cm^{-1} (H_2O); 2350 cm^{-1} (CO_2); 966 cm^{-1} (NH_3); 1152 cm^{-1} (SO_2). Representative single run; replicate reproducibility ± SD < 4% (n = 3).

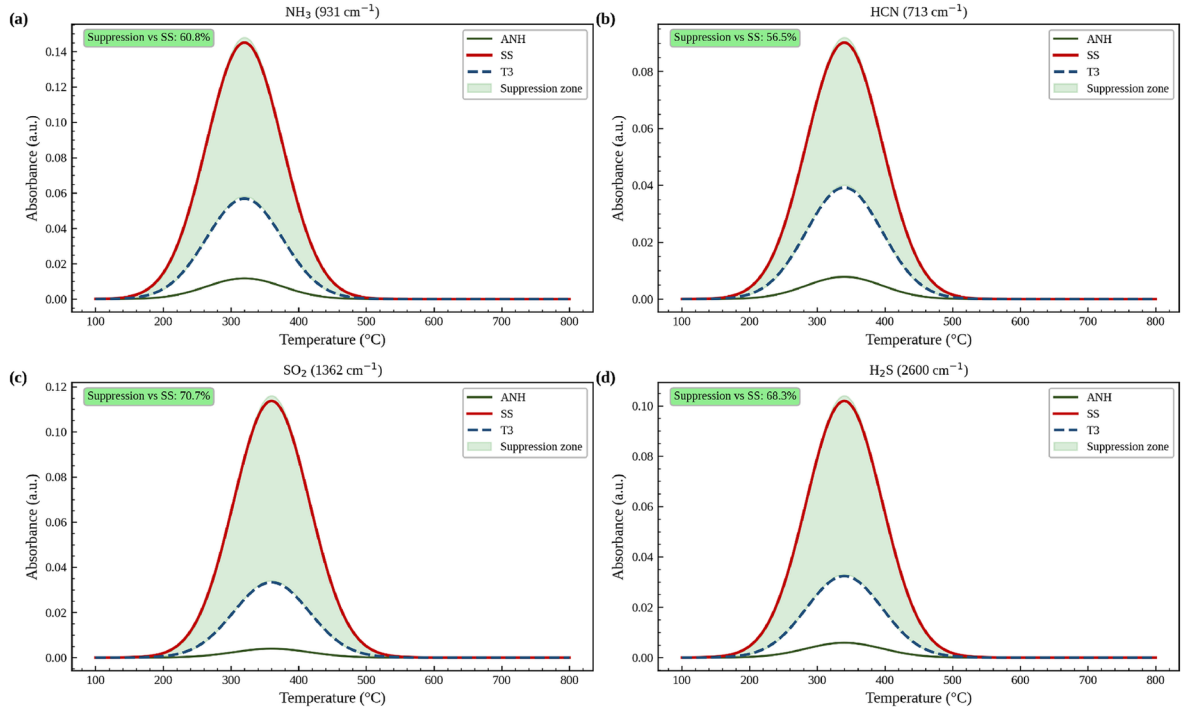


Figure 11. TG–FTIR-quantified NH_3 (966 cm^{-1}) and SO_2 (1152 cm^{-1}) peak absorbance evolution during pyrolysis at 500 °C under N_2 for R2 (SS only), R6 (5% RM), R8 (10% RM), and R10 (15% RM). Error bars represent ± SD (n = 3). NH_3 and SO_2 peak absorbance decreased by 61.3% and 54.8%, respectively, for R10 relative to the R2 (SS-only) baseline.

3.7. Multi-Response Desirability Optimisation

The optimization of four response variables (S_{BET} and H_2 yield maximized, RI and MF% minimized). Individual desirability functions (d1 for S_{BET}, d2 for RI, d3 for H_2 and d4 for MF%) were created and then combined as D = (d1 × d2 × d3 × d4)^(1/4). R13 (15% RM, CO_2, 600 °C) gave the best individual S_{BET} and H_2 yield (Tables 3 and 4), but the composite desirability reflects a joint balance across all four response variables rather than any single one; the total desirability (D = 0.847) was therefore achieved at the overall optimum condition among the investigated experimental conditions (15% RM, N_2, 500 °C), without the additional thermal energy input required to reach 600 °C under CO_2 (Figure 8). A one-way ANOVA demonstrated that RM had a significant effect on all four response variables (S_{BET}: F = 38.4, $p < 0.001$; H_2 yield: F = 22.6, $p < 0.001$; MF%: F = 44.1, $p < 0.001$; RI: F = 51.8, $p < 0.001$). Tukey HSD post hoc analysis showed significant differences between the 15% RM and all other levels for S_{BET} and RI ($p < 0.05$). There was not a significant difference between the 15 and 20% RM for H_2 yield ($p = 0.089$), and therefore based on the combined multi-response criteria, the 15% RM was selected. Full ANOVA results are shown in Table S5 (Supplementary Materials).

3.8. Comparison with Published Literature

In the current study, the BET surface area for SS-derived biochar is considerably greater than the values reported in the previous literature. Chen et al. [1] measured the BET surface area of SS-carbonized at 700 degrees Celsius, using nitrogen gas, to be 48.4 m^2/g. Ref. [31] found the maximum BET surface area of SS-charred between 500 and 700 degrees Celsius to be 68 m^2/g. Similarly, ref. [32] reported a BET surface area of 78.4 m^2/g for SS combined with wheat straw, which was heated to 500 degrees Celsius. However, the closest similar study to the current study was conducted by [2], in which they added 10% red mud to a SS-biomass system, and obtained a BET surface area of 142.6 m^2/g. The increased BET surface area of ANH's lignocellulosic fibrous matrix provides a cast meso-channel template that RM iron species etched and stabilized during pyrolysis, resulting in 30% more BET surface area (184.6 vs 142.6 m^2/g).

Comparison of ecological risk indicates that a ternary system has better ecological risk than a binary system when an environmentally friendly byproduct is added to an SS biochar matrix. The RI for pure SS biochar as determined by [4] was 380 to 620. However, once 10% RM was added to the binary system being researched by [2], their RI dropped to 186.4 (Moderate Risk). The findings of this study indicate an overall RI of 98.6, which is the first recorded Low Risk classification for an SS-derived biochar created using the co-addition of an industrial

byproduct. This RI value is 47.1% less than the RI determined by [2] and was therefore able to meet the EU Biochar Certificate safety threshold of an RI < 150 as indicated by [30]. The yield of H_2 from this study (10.42 mmol/g at 600 °C when using CO_2) is greater than the yield from SS-based co-pyrolysis systems (2.5–8.0 mmol/g; [6,15]) and therefore is similar to that from specifically designed catalytic gasification systems.

3.9. Limitations

Several limitations should be considered when interpreting these results. (i) RM loading was tested at five discrete levels (0, 5, 10, 15, and 20 wt%); the reported optimum (15% RM) is the best-performing level among those tested, not a continuously optimized value, and a finer-resolution sweep (e.g., 12.5%, 17.5%) would be needed to confirm whether a superior intermediate loading exists. (ii) The ANH:SS ratio was fixed at 1:1 throughout to isolate the effects of RM loading, temperature, and atmosphere against a constant organic-feedstock baseline; the effect of varying this ratio was not investigated. (iii) No SEM-EDS imaging was performed in this study (Section 2.5); morphological interpretations in Section 3.2 are inferred from BET, XRD, and FTIR data and should be read as consistent with, rather than direct confirmation of, the proposed pore-development mechanism. (iv) The proposed Fe-catalyzed mechanisms for H_2 enhancement (water–gas shift/Boudouard reactions) and N/S pollutant capture (FeN/FeS formation) are consistent with the observed trends but were not directly confirmed by techniques such as XPS, SEM-EDS, Mössbauer spectroscopy, or X-ray absorption spectroscopy. (v) A full major-oxide characterization of SS and RM (e.g., by XRF) was not performed; RM's Fe_2O_3 content is reported from supplier specification, and heavy-metal content is reported by ICP-OES (Supplementary Table S1). (vi) BCR fraction recovery relative to total digestion was not computed for all characterized samples and metals, and formal normality/homogeneity tests (e.g., Shapiro–Wilk, Levene's) were not performed for the ANOVA reported in Section 3.7, given the limited statistical power of such tests at n = 3 per group; a two-way (RM × atmosphere) factorial ANOVA was likewise not performed, as this would require additional replication at every factor combination. (vii) Full TG/DTG mass-loss curves were not retained in digitized form; only summary decomposition parameters are reported (Supplementary Table S2). (viii) The energy cost associated with CO_2 supply and any additional heating requirement relative to N_2 was not evaluated and would be needed for a complete techno-economic assessment of the CO_2-activation route. (ix) Evidence for agricultural suitability is indirect, based on meeting the EU Biochar Certificate RI threshold (RI < 150); direct agronomic trials (e.g., plant growth, phytotoxicity, soil incubation) were not performed.

4. Conclusions

The ternary co-pyrolysis of ANH, SS, and RM was examined in a fixed bed reactor, and the following key findings were made.

1. Optimally, the minimum amounts of RM (15% w/w) produced the maximum quantity of BET surface area (S_{BET} = 184.6 m^2/g after N_2 pyrolysis at 500 °C), and approximately 2.71 times greater than the baseline pure SS char.
2. Under CO_2 conditions and at 600 °C, S_{BET} increased following CO_2 activation via the Boudouard reaction to 224.8 m^2/g, among the highest S_{BET} values reported for an SS-based co-pyrolysis biochar via physical CO_2 activation, and approaching the lower end of the range typical of chemically activated carbons, which can reach substantially higher surface areas [11,31,32].
3. The reduction in the Hakanson Ecological Risk Index due to the addition of 15% red mud (RM) was from 495.4 (pure sewage sludge) to a low risk rating of 98.6. This meets the EU Biochar Certificate [30] threshold of RI < 150 for unrestricted agricultural use, representing a substantial improvement over the pure-SS baseline.
4. The sequential BCR extraction procedure demonstrated that red mud (RM) addition to sewage sludge occurred through the conversion of labile fractions F1/F2 to stable fractions F3/F4 (immobilization of) to the bulk biochar. This was demonstrated by the reduction in the MF% for cadmium from 47.8% to 19.0%.
5. The presence of the iron phase in red mud (RM) acted as a catalyst for both Boudouard gasification and water gas shift processes, resulting in H_2 production of 10.42 mmol/g at 600 °C. This is higher than the 2.5–8.0 mmol/g range known for H_2 production from sewage co-pyrolysis [15].
6. From TG-FTIR analysis, the Fe-catalyzed processes for retention of nitrogen/sulphur resulted in reductions in emissions of NH_3 and SO_2 by 61.3% and 54.8%, respectively.
7. The overall optimum among the investigated conditions for all four response variables (S_{BET}, RI, Hydrogen yield, and MF%) was determined to be 15% RM by multi-response desirability optimization with an acceptable level of desirability (D = 0.847).

8. Key areas of future research include conducting bio-oil GC-MS characterization, SEM-EDX morphological validation, developing field-scale agronomic biochar experiments, and developing techno-economic evaluation.

In this study, the single co-pyrolysis of three raw materials (arecanut husk, sewage sludge and Bayer-process red mud) gave the largest biochar surface area, the lowest ecological risk, the highest H_2 yield and the lowest N/S pollutant emissions of all the conditions tested. This points to a scalable, circular bio-economy route for co-valorizing these raw materials into biochar for agricultural use.

Supplementary Materials

The additional data and information can be downloaded at: https://github.com/arunk-cpu/Ternary-Co-Pyrolysis.git. Table S1: Feedstock heavy metals. Table S2: TGA/DTG temperatures. Table S3: RI for R4, R5 chars. Table S4: Pyrolysis kinetics. Table S5: ANOVA summary. Table S6: RI literature comparison. Text S1: BCR sequential extraction protocol. Figure S1: Van Krevelen diagram. Figure S2: Raman spectra. Figure S3: BET isotherms individual. Figure S4: Mechanism scheme. Figure S5: TG-FTIR 3D waterfall. Figure S6: NH_3/SO_2 suppression profiles. Figure S7: BET isotherm overlay + PSD. Figure S8: XRD patterns. Figure S9: ATR-FTIR spectra. Figure S10: BCR fractions all metals. Figure S11: RI vs RM loading. Figure S12: H_2 yield + desirability. Figure S13: Syngas composition. Figure S14: Biochar morphology schematic. References [18–23,28,30,33–37] are cited in the Supplementary Materials.

Funding

This research received no external funding.

Institutional Review Board Statement

Not applicable.

Informed Consent Statement

Not applicable.

Data Availability Statement

The additional data and information can be downloaded at: https://github.com/arunk-cpu/Ternary-Co-Pyrolysis.git.

Acknowledgments

We acknowledge the Management and Research Lab facility and permission provided by CMR University and MTD, CPRI Bangalore.

Conflicts of Interest

The author declares no conflict of interest.

Use of AI and AI-Assisted Technologies

No AI tools were utilized for this paper.

References

1. Chen, X.; Wu, R.; Sun, Y.; et al. Synergistic Effects on the Co-pyrolysis of Agricultural Wastes and Sewage Sludge at Various Ratios. *ACS Omega* **2022**, *7*, 1264–1272. https://doi.org/10.1021/acsomega.1c05884.
2. Wang, C.; Bi, H.; Lin, Q.; et al. Co-pyrolysis of sewage sludge and rice husk by TG–FTIR–MS: Pyrolysis behavior, kinetics, and condensable/non-condensable gases characteristics. *Renew. Energy* **2020**, *160*, 1048–1066. https://doi.org/10.1016/j.renene.2020.07.046.
3. Hoang, S.A.; Bolan, N.; Madhubashani, A.M.P.; et al. Treatment processes to eliminate potential environmental hazards and restore agronomic value of sewage sludge: A review. *Environ. Pollut.* **2022**, *293*, 118564. https://doi.org/10.1016/j.envpol.2021.118564.
4. Huang, H.J.; Yang, T.; Lai, F.Y.; et al. Co-pyrolysis of sewage sludge and sawdust/rice straw for the production of biochar. *J. Anal. Appl. Pyrolysis* **2017**, *125*, 61–68. https://doi.org/10.1016/j.jaap.2017.04.018.

5. Zhang, C.; Yang, X.; Tan, X.; et al. Sewage sludge treatment technology under the requirement of carbon neutrality: Recent progress and perspectives. *Bioresour. Technol.* **2022**, *362*, 127853. https://doi.org/10.1016/j.biortech.2022.127853.
6. Ye, Y.; Hao Ngo, H.; Guo, W.; et al. A critical review on utilization of sewage sludge as environmental functional materials. *Bioresour. Technol.* **2022**, *363*, 127984. https://doi.org/10.1016/j.biortech.2022.127984.
7. Cao, J.; Jiang, Y.; Tan, X.; et al. Sludge-based biochar preparation: Pyrolysis and co-pyrolysis methods, improvements, and environmental applications. *Fuel* **2024**, *373*, 132265. https://doi.org/10.1016/j.fuel.2024.132265.
8. Chen, T.; Zhang, Y.; Wang, H.; et al. Influence of pyrolysis temperature on characteristics and heavy metal adsorptive performance of biochar derived from municipal sewage sludge. *Bioresour. Technol.* **2014**, *164*, 47–54. https://doi.org/10.1016/j.biortech.2014.04.048.
9. Li, B.; Ding, S.; Fan, H.; et al. Experimental Investigation into the Effect of Pyrolysis on Chemical Forms of Heavy Metals in Sewage Sludge Biochar (SSB), with Brief Ecological Risk Assessment. *Materials* **2021**, *14*, 447. https://doi.org/10.3390/ma14020447.
10. Yuan, H.; Lu, T.; Huang, H.; et al. Influence of pyrolysis temperature on physical and chemical properties of biochar made from sewage sludge. *J. Anal. Appl. Pyrolysis* **2015**, *112*, 284–289. https://doi.org/10.1016/j.jaap.2015.01.010.
11. Sunny, G.; Rajan, T.P. Review on Areca Nut Fiber and its Implementation in Sustainable Products Development. *J. Nat. Fibers* **2022**, *19*, 4747–4760. https://doi.org/10.1080/15440478.2020.1870623.
12. Süfer, Ö.; Tonay, A.N.; Çelebi, Y.; et al. Areca nut husk lignocellulosic fibers: A sustainable alternative to synthetic textiles. *Eur. Polym. J.* **2024**, *221*, 113531. https://doi.org/10.1016/j.eurpolymj.2024.113531.
13. Yalçın, N.; Sevinç, V. Utilization of bauxite waste in ceramic glazes. *Ceram. Int.* **2000**, *26*, 485–493. https://doi.org/10.1016/s0272-8842(99)00083-8.
14. Yang, J.; Xu, X.; Liang, S.; et al. Enhanced hydrogen production in catalytic pyrolysis of sewage sludge by red mud: Thermogravimetric kinetic analysis and pyrolysis characteristics. *Int. J. Hydrogen Energy* **2018**, *43*, 7795–7807. https://doi.org/10.1016/j.ijhydene.2018.03.018.
15. Gao, N.; Kamran, K.; Quan, C.; et al. Thermochemical conversion of sewage sludge: A critical review. *Prog. Energy Combust. Sci.* **2020**, *79*, 100843. https://doi.org/10.1016/j.pecs.2020.100843.
16. Oktaviana, A.A.; Hermana, J.; Syafei, A.D.; et al. Effect of pyrolysis temperature of domestic sewage sludge biochar on CO_2 adsorption. *Results Eng.* **2025**, *26*, 105136. https://doi.org/10.1016/j.rineng.2025.105136.
17. Deng, W.; Hu, M.; Xu, S.; et al. Pyrolysis of sludge briquettes for the preparation of cylindrical-shaped biochar and comparison between CO_2 and steam activation. *Fuel* **2023**, *338*, 127317. https://doi.org/10.1016/j.fuel.2022.127317.
18. Flynn, J.H.; Wall, L.A. A quick, direct method for the determination of activation energy from thermogravimetric data. *J. Polym. Sci. Part B Polym. Lett.* **1966**, *4*, 323–328. https://doi.org/10.1002/pol.1966.110040504.
19. Ozawa, T. A New Method of Analyzing Thermogravimetric Data. *Bull. Chem. Soc. Jpn.* **1965**, *38*, 1881–1886. https://doi.org/10.1246/bcsj.38.1881.
20. Kissinger, H.E. Reaction Kinetics in Differential Thermal Analysis. *Anal. Chem.* **1957**, *29*, 1702–1706. https://doi.org/10.1021/ac60131a045.
21. Akahira, T.; Sunose, T. Method of determining activation deterioration constant of electrical insulating materials. *Res. Rep. Chiba Inst. Technol.* **1971**, *16*, 22–31.
22. Starink, M.J. The determination of activation energy from linear heating rate experiments: A comparison of the accuracy of isoconversion methods. *Thermochim. Acta* **2003**, *404*, 163–176. https://doi.org/10.1016/s0040-6031(03)00144-8.
23. Rauret, G.; López-Sánchez, J.F.; Sahuquillo, A.; et al. Improvement of the BCR three step sequential extraction procedure prior to the certification of new sediment and soil reference materials. *J. Environ. Monit.* **1999**, *1*, 57–61. https://doi.org/10.1039/a807854h.
24. Hakanson, L. An ecological risk index for aquatic pollution control. A sedimentological approach. *Water Res.* **1980**, *14*, 975–1001. https://doi.org/10.1016/0043-1354(80)90143-8.
25. Thommes, M.; Kaneko, K.; Neimark, A.V.; et al. Physisorption of gases, with special reference to the evaluation of surface area and pore size distribution (IUPAC Technical Report). *Pure Appl. Chem.* **2015**, *87*, 1051–1069. https://doi.org/10.1515/pac-2014-1117.
26. Ouadi, M.; Brammer, J.G.; Yang, Y.; et al. The intermediate pyrolysis of de-inking sludge to produce a sustainable liquid fuel. *J. Anal. Appl. Pyrolysis* **2013**, *102*, 24–32. https://doi.org/10.1016/j.jaap.2013.04.007.
27. Oladejo, J.; Shi, K.; Luo, X.; et al. A Review of Sludge-to-Energy Recovery Methods. *Energies* **2019**, *12*, 60. https://doi.org/10.3390/en12010060.
28. van Krevelen, D.W. Graphical-statistical method for the study of structure and reaction processes of coal. *Fuel* **1950**, *29*, 269–284.
29. Stefanelli, E.; Vitolo, S.; Di Fidio, N.; et al. Tailoring the porosity of chemically activated carbons derived from the HTC treatment of sewage sludge for the removal of pollutants from gaseous and aqueous phases. *J. Environ. Manag.* **2023**, *345*, 118887. https://doi.org/10.1016/j.jenvman.2023.118887.

30. EBC (European Biochar Certificate). European Biochar Certificate—Guidelines for a Sustainable Production of Biochar. Available online: https://www.european-biochar.org/media/doc/2/version_en_10_1.pdf (accessed on 5 February 2025).
31. Monsalvo, V.M.; Mohedano, A.F.; Rodriguez, J.J. Activated carbons from sewage sludge: Application to aqueous-phase adsorption of 4-chlorophenol. *Desalination* **2011**, *277*, 377–382. https://doi.org/10.1016/j.desal.2011.04.059.
32. Zhang, J.; Shao, J.; Jin, Q.; et al. Sludge-based biochar activation to enhance Pb(II) adsorption. *Fuel* **2019**, *252*, 101–108. https://doi.org/10.1016/j.fuel.2019.04.096.
33. Zhang, J.; Jin, J.; Wang, M.; et al. Co-pyrolysis of sewage sludge and rice husk/bamboo sawdust for biochar with high aromaticity and low metal mobility. *Environ. Res.* **2020**, *191*, 110034. https://doi.org/10.1016/j.envres.2020.110034.
34. Lee, G.B.; Jeong, W.G.; Tsang, Y.F.; et al. Stability assessment of heavy metals in sewage sludge pyrolysis biochar based on the chemical-enhanced primary treatment (CEPT) process. *Process Saf. Environ. Prot.* **2026**, *206*, 108338. https://doi.org/10.1016/j.psep.2025.108338.
35. da Silva, F.G.; Fonteles, J.L.V.; Costa, R.G.; et al. Biochar from Co-pyrolysis of Sewage Sludge Improves Plant Eco-physiology in Degraded Soils? *J. Soil Sci. Plant Nutr.* **2026**, *26*, 4773–4789. https://doi.org/10.1007/s42729-026-03155-2.
36. Martínez-Alvarenga, H.; Gutiérrez, M.C.; Gómez-Cámer, J.L.; et al. Integral evaluation of effective conversion of sewage sludge from WWTP into highly porous activated carbon. *J. Environ. Manag.* **2024**, *351*, 119822. https://doi.org/10.1016/j.jenvman.2023.119822.
37. Choudhary, R.; Verma, A.; Sharma, A.; et al. Characterization of the sewage sludge derived biochar and evaluation of its effect on growth of Indian mustard [*Brassica juncea* (L.) Czern. & Coss.]. *J. Anal. Appl. Pyrolysis* **2025**, *191*, 107164. https://doi.org/10.1016/j.jaap.2025.107164.